(Received 28 October 2025, Accepted 10 December 2025, Scheduled 9 January 2026)

Design of a Radiation Error Correction Algorithm for Four-Wire Sounding Temperature Sensor

Yu Tong Liu[1], Ren Hui Ding[2,*], Zheng Jie Ying[1], and Jia Le Jiang[1]

[1] School of Electronic and Information Engineering, Nanjing University of Information Science and Technology, 210044, China
[2] Jiangsu Meteorological Observation Center, 210041, China

ABSTRACT: To ensure adequate ventilation, radiosonde temperature sensors are typically mounted on top of the device and directly exposed to solar radiation. However, this configuration makes the sensors highly susceptible to radiation-induced errors, which can significantly compromise temperature measurement accuracy. This study proposes a four-wire structural design for the radiosonde temperature sensor and evaluates its performance through computational fluid dynamics (CFD) simulations. The radiosonde follows a helical ascent trajectory, which causes the incident solar radiation on the sensor to vary continuously. This continuous variation makes the quantification and correction of radiation errors more difficult. The proposed four-wire design achieves favorable radiative thermal balance in three-dimensional space. It also demonstrates low sensitivity to changes in the ascent trajectory. This characteristic allows the correction model to be simplified by neglecting variations in the incident radiation direction. A coupled flow-structure thermal analysis is conducted under varying environmental conditions, including altitude, ascent velocity, and solar radiation intensity, to quantify the radiation error of the four-wire sensor. A neural network algorithm is then trained on the simulation data to develop a radiation error correction model. Experimental validation is performed using a platform comprising a full-spectrum solar simulator and a low-pressure wind tunnel. The experimental results yield a root mean square error (RMSE) of 0.159 K, mean absolute error (MAE) of 0.143 K, and correlation coefficient of 0.962 between simulated and corrected radiation errors, demonstrating the high accuracy of the proposed correction algorithm. After correction, the average radiation error of the four-wire sensor decreases from 0.446 K to 0.143 K, substantially improving temperature measurement accuracy.

1. INTRODUCTION

Accurate and timely vertical atmospheric temperature observations are essential for characterizing temperature distributions at various altitudes and provide critical data for weather forecasting and climate change analysis [1]. High-altitude temperature measurements also play a key role in extreme weather warnings [2–4], environmental monitoring [5–7], and natural disaster risk assessment. At present, radiosondes — equipped with sensors to measure temperature, humidity, and pressure in real time — remain the primary tools for upper-atmosphere meteorological observations. To ensure adequate ventilation during ascent, temperature sensors are typically mounted at the top of the radiosonde, directly exposed to solar radiation. However, this configuration introduces significant radiation-induced errors, causing temperature readings to exceed actual ambient values and reducing the accuracy and reliability of radiosonde data. According to the World Meteorological Organization (WMO) Guidelines for Meteorological Instruments and Methods of Observation, the measurement uncertainty of modern radiosondes typically ranges from 0.4 K to 1 K and may exceed 2 K in tropical regions [8]. Moreover, as the radiosonde ascends along a helical trajectory, the incident solar radiation on the sensor varies continuously, further complicating radiation error correction. These radiation-induced biases have become a major limiting factor in the performance of radiosonde temperature sensors. Therefore, effective mitigation of radiation errors remains a critical challenge in current high-altitude meteorological and climate research [9].

Radiosonde temperature sensors include a variety of types, such as platinum resistance thermometers, bead thermistors, rod thermistors, film thermistors, helical sensors, and thermocouples. Among them, bead thermistors are widely used in atmospheric sounding due to their favorable thermal response characteristics [10, 11]. Typically composed of spherical or ellipsoidal ceramic-sintered resistive elements with diameters ranging from 0.6 mm to over 2 mm, bead thermistors are coated with aluminum film or white paint for protection and are electrically connected via two rear-mounted leads [12]. In recent years, the diameter of these sensors has been reduced to less than 1 mm, effectively decreasing solar radiation absorption and enhancing convective heat exchange with the surrounding air [13, 14]. These improvements have significantly enhanced their measurement accuracy under varying environmental conditions, making bead thermistors one of the most commonly used temperature sensors in radiosonde applications [15].

To mitigate radiation-induced errors, extensive research has focused on structural optimization of radiosonde temperature sensors. For example, Wang et al. developed a novel microbridge temperature sensor and conducted simulation analyses to evaluate the effects of Joule heating, solar radiation, and aerodynamic heating on temperature errors, achieving a sub-

* Corresponding author: Ren Hui Ding (15062233858@163.com).

TABLE 1. Comparative results of solar radiation error correction methods reported in previous studies.

Reference	Description	Metrics
This paper	The radiation error was computed using CFD simulations. Based on the structuralcharacteristics of the four-wire sensor, an MLP model was developed to correct the radiation error, and the model was experimentally validated using a solar simulator and a low-pressure wind tunnel.	The algorithm reduced the mean error from 0.446 K to 0.143 K.
18	Using a UAS to simulate the upper-air environment, a radiation-correction model incorporating parameters such as T, P, v, and S was developed. By performing uncertainty propagation and boom-attitude compensation, the radiation-corrected temperature of the RS41 was obtained.	The expanded uncertainty of the radiation-corrected temperature (with a coverage factor of $k = 2$, corresponding to a confidence level of approximately 95%) is 0.17°C.
21	Using a simulation setup, the radiation error was systematically characterized experimentally, and a two-dimensional parameterized model of the radiation error was established.	After correction, the radiation error varies from 0.1 to 0.8 K with altitude.
22	Radiation biases were identified using RO, ERA5, and dual-sonde references, and a GRUAN temperature correction was developed based on solar zenith angle and pressure, enabling the correction of radiation errors in the RS92/RS41 GDP.2 products.	The GRUAN correction method can reduce the bias by approximately 0.5 K at 20 hPa during daytime.

stantial reduction in solar radiation-induced bias [13]. Liu et al. improved sensor response time and measurement accuracy by incorporating insulating layers and reflective encapsulation in the design of bead thermistors [12]. Lee et al. proposed a calibration method using two thermistors coated with different materials to estimate radiation intensity, offering a simple and effective approach to solar radiation compensation [16, 17]. In general, strategies, such as employing small-sized, low-heat-capacity bead thermistors, and applying reflective surface coatings, have helped reduce radiation errors to a certain extent [18]. However, these improvements remain limited. At high altitudes, rapid fluctuations in solar radiation and variations in the sensor's effective receiving area — caused by radiosonde attitude instability during ascent — continue to introduce significant uncertainty. Consequently, structural optimization alone is insufficient to meet the demands of high-precision atmospheric temperature measurements.

Radiation error correction methods in research have largely relied on simplified models that use macro-level parameters — such as altitude, solar radiation intensity, atmospheric pressure, and time — to construct empirical or semi-empirical regression models [19, 20]. For instance, von Rohden et al. proposed a correction model in which the estimated radiation error increased from 0.1 K at ground level to 0.8 K at an altitude of 35 km [21]. Jing et al. developed a correction method for RS92 and RS41 radiosondes, achieving an error reduction of approximately 0.5 K under daytime conditions at 20 hPa [22]. Lee et al. utilized a high-altitude meteorological simulator to investigate the effects of solar radiation, reporting that the uncertainty of RS41-corrected temperatures was 0.17 K at the 95% confidence level [18]. A common limitation of these models is the assumption of vertical radiosonde ascent, disregarding changes in sensor attitude and orientation due to three-dimensional wind field disturbances during actual flight. These dynamic variations cause continuous changes in the sensor's effective exposure to solar radiation — a factor strongly correlated with radiation error. Ignoring this variability significantly restricts the accuracy and adaptability of existing correction models. As a result, many of these methods perform poorly under real-world radiosonde flight conditions, especially in dynamically evolving atmospheric environments. Therefore, to improve the accuracy of high-altitude temperature measurements, it is essential to pursue advances in both structural sensor design and radiation error correction methodology. Table 1 summarizes the comparative results of solar radiation error correction methods reported in previous studies.

In this study, a four-wire radiosonde temperature sensor is proposed, featuring a structural design that offers excellent radiative thermal balance. The sensor maintains a stable radiative heat exchange in three-dimensional space, rendering the received radiation flux relatively insensitive to attitude variations during ascent. This characteristic allows dynamic changes in the irradiated surface to be neglected during error correction, significantly reducing the complexity of correction model development. Computational Fluid Dynamics (CFD) is employed to perform coupled flow-structure-thermal simulations under various environmental conditions, including ascent velocity, total solar radiation intensity, and altitude [23]. The simulations yield a high-precision radiation error dataset. A neural network algorithm is then trained on this dataset to construct a radiation error correction model [24]. Finally, experimental validation of both the four-wire sensor and the correction algorithm is carried out using a high-altitude environmental simulation platform comprising a full-spectrum solar simulator and a low-pressure wind tunnel. Compared with previous studies on radiosonde temperature sensors, this work further enhances the sensor's radiative thermal balance through structural optimization and introduces an integrated correction framework that combines CFD simulation data with a neural network model, thereby significantly improving the measurement accuracy after radiation error correction.

TABLE 2. Comparison of mesh division parameters, number of mesh elements, and radiation error simulation results for different mesh models.

Mesh scheme	Minimum mesh size (mm)	Curvature normal angle (°)	Number of mesh elements (10^4)	Radiation error simulation result (K)
Coarse #2	0.2	18	42	0.292
Coarse #1	0.1	18	59	0.323
Baseline	0.05	18	76	0.339
Refined #1	0.03	15	102	0.341
Refined #2	0.02	15	169	0.342

2. MULTIPHYSICS HEAT TRANSFER ANALYSIS FOR THE FOUR-WIRE RADIOSONDE TEMPERATURE SENSOR

2.1. Construction of the 3D Physical and Mesh Models of the Four-Wire Sensor

The three-dimensional physical model of the four-wire temperature sensor consists of a miniature bead thermistor positioned at its center, encapsulated in an epoxy layer to provide mechanical protection and environmental isolation. The sensing element is supported by four slender metallic leads arranged in a symmetric cross configuration. Each lead has a diameter of 0.2 mm and a length of 15 mm, providing sufficient mechanical rigidity while minimizing thermal expansion effects. The exterior of the sensor is coated with an aluminum layer, which effectively reflects incident solar radiation and further reduces radiative heating. Geometrically, the four leads are uniformly distributed at 90° intervals in the azimuthal direction, forming a highly symmetric three-dimensional support structure that promotes directional equilibrium of radiative heat flux. This symmetry substantially reduces the sensor's sensitivity to changes in solar incidence angle caused by radiosonde rotation or pendulum-like oscillation during ascent, thereby enhancing measurement stability under radiative heating conditions. In the experimental setup, the sensor is mounted such that the plane of the leads is perpendicular to the direction of incoming solar radiation, ensuring uniform radiative exposure across all leads. The thermistor is fully exposed to both radiation and airflow without any additional shielding, replicating its actual operating configuration during radiosonde flights. The three-dimensional structural model of the sensor is shown in Fig. 1.

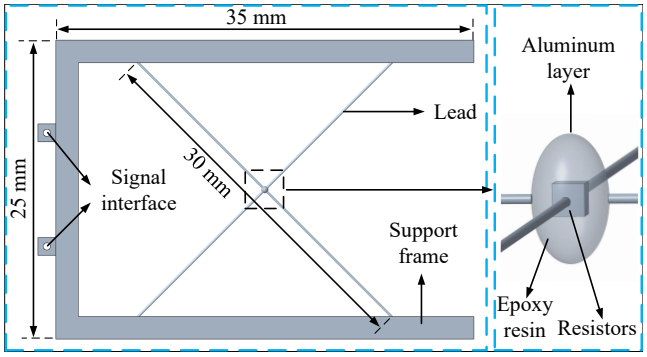

FIGURE 1. 3D physical model of the four-wire temperature sensor.

To ensure convergence and physical consistency of the simulation results, an appropriately sized computational domain is critical. Considering the radiosonde temperature sensor operates within an effectively infinite air domain, a cubic computational domain with dimensions approximately ten times the sensor's characteristic length was employed to approximate the unbounded environment. This choice balances computational accuracy with efficiency. The sensor model is positioned at one-third of the domain length from the inlet boundary in the downstream direction, minimizing boundary effects on the flow field around the sensor. The physical model of the four-wire radiosonde temperature sensor and its surrounding air domain is illustrated in Fig. 2(b). In this model, the left boundary serves as the airflow inlet, representing the upstream position relative to the radiosonde, while the right boundary is set as the airflow outlet. To guarantee sufficient airflow development, the air domain extends along the flow path. During mesh generation, an unstructured hybrid meshing approach was applied using ICEM CFD, incorporating localized refinement near critical regions. These include the temperature-sensing element surface, the junctions of the supporting leads, and areas prone to flow separation or vortex formation upstream and downstream of the sensor. This refinement enables accurate resolution of microscale thermal flow and heat transfer phenomena, which is essential for reliable and physically meaningful CFD simulations in radiation error evaluation. Fig. 2(a) presents the mesh model of the sensor alone, while Figs. 2(a) (b) show the mesh encompassing both the four-wire sensor structure and its surrounding air domain.

In constructing a high-quality mesh model for the four-wire radiosonde temperature sensor, a rational control of mesh distribution is essential to balance simulation efficiency and modeling accuracy. To accurately resolve the sensor's complex geometry and the physical field variations in the surrounding fluid domain, while avoiding the excessive computational cost of uniformly fine meshes, a differentiated mesh size control strategy is employed. This strategy integrates curvature-based refinement with soft size control to optimize mesh quality. In regions with sharp geometric features — such as the spherical surface of the temperature-sensing element, the intersections of the four leads, and the sensor support structure — a curvature control algorithm dynamically adjusts mesh density according to local curvature. This targeted refinement enhances mesh resolution and quality in critical areas. Conversely, in air regions distant from the sensor, where physical gradients are relatively mild, a soft size control method imposes an up-

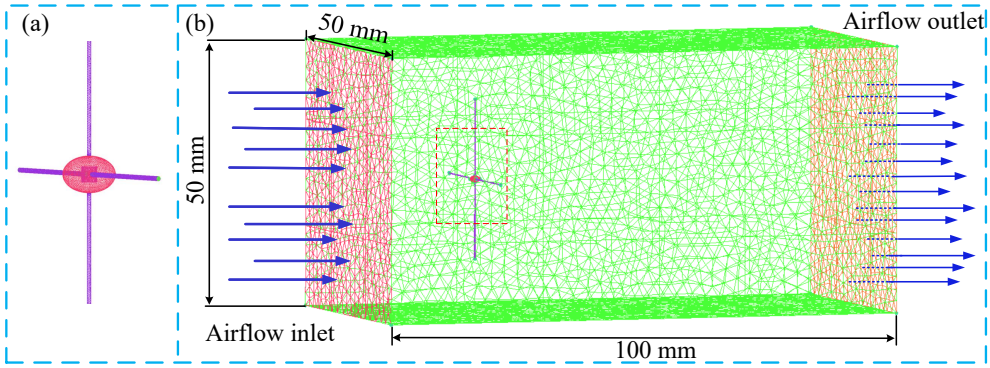

FIGURE 2. (a) Mesh model of the four-wire radiosonde temperature sensor. (b) Mesh model of the sensor and its surrounding air domain.

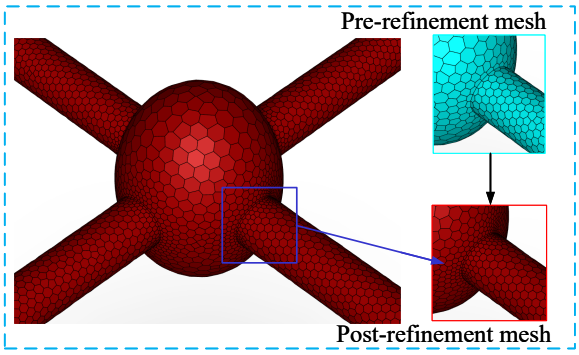

FIGURE 3. Comparison of mesh refinement before and after applying curvature control in localized regions.

per limit on mesh size, effectively reducing the total cell count and lowering computational demands. The combined application of these methods achieves global optimization of the three-dimensional mesh, ensuring strong adaptability and precision in capturing the coupled thermal-fluid phenomena. Fig. 3 illustrates the local mesh refinement before and after applying the curvature control algorithm, demonstrating significant improvement in mesh quality [25, 26].

To verify the stability and convergence of the numerical simulations for the four-wire radiosonde temperature sensor under varying mesh resolutions and to ensure the accuracy and reliability of the results, a systematic grid independence study was performed. Starting from the baseline mesh optimized using curvature and soft size control, two levels of mesh refinement and two levels of coarsening were applied, resulting in five representative grid configurations. All cases maintained consistent geometry and boundary conditions, with flow and heat transfer simulations conducted in ANSYS Fluent. Key evaluation metrics included the surface temperature distribution and local flow field parameters. As summarized in Table 2, the temperature of the resistive element showed gradual convergence as the mesh cell count increased. Once the total number of mesh cells exceeded 76 million, the variation in simulation results fell below 3%, indicating that further mesh refinement had a negligible impact on the solution. Consequently, this mesh configuration was selected for all subsequent simulations [27].

2.2. Multi-Physics Simulation Model Construction

To systematically investigate the thermal response characteristics of the four-wire radiosonde temperature sensor under high-altitude solar radiation conditions, a multiphysics coupled numerical simulation was conducted using ANSYS Fluent [28]. The finite volume method was employed to discretize both the sensor geometry and the surrounding air domain. The computational mesh incorporated localized refinement near the thermistor surface, lead junctions, and upstream/downstream regions prone to flow separation or vortex formation. The minimum mesh size was set to 0.05 mm, and curvature-based mesh refinement was controlled with a normal angle of 18° to accurately capture complex geometrical features. The left boundary was set as a velocity inlet corresponding to the sensor ascent speed, the right boundary as a pressure outlet, and all other faces as adiabatic no-slip walls. A pressure-based steady solver was selected, with velocity-pressure coupling achieved via the SIMPLE algorithm. The energy equation was fully solved to account for the thermal effects of solar radiation. The standard k-ε turbulence model was applied to capture boundary layer behavior and turbulent heat transfer, while the Discrete Ordinates model was used for radiative heat transfer from solar irradiation. A first-order upwind discretization was used in initial iterations to promote convergence, followed by a second-order upwind scheme for momentum, energy, and turbulence once the solution stabilized.

The simulation conditions were defined as follows: solar radiation intensity of 1000 W/m^2, sensor ascent velocity of 5 m/s, simulated altitude of 30 km, and sensor surface reflectivity of 0.85. In addition, the model incorporated an altitude-dependent atmospheric profile based on the International Standard Atmosphere (ISA). The ambient temperature decreases with altitude, following the standard lapse rate of -6.5 K/km, while the pressure and air density are computed as functions of altitude using the hydrostatic equation and the ideal gas law, respectively. To evaluate the effect of solar incident angle on thermal performance, CFD simulations were performed under varying irradiation directions. The solar radiation was initialized at a 45° angle relative to the XOZ plane and the Z-axis, then rotated around the sensor in 30° increments to encompass directions up to the YOZ plane. For each irradiation setting, all other

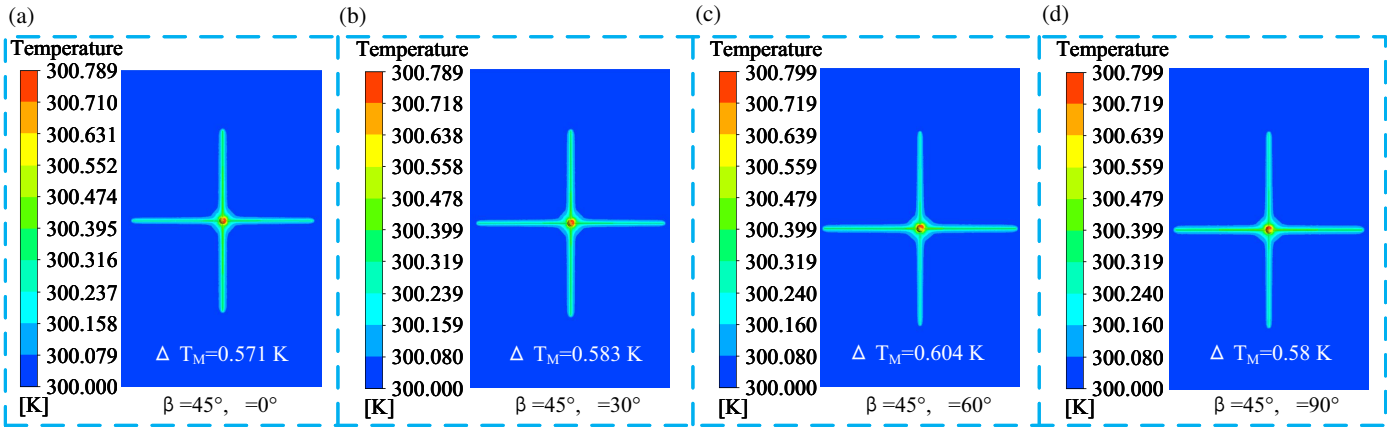

FIGURE 4. Temperature field distribution of the four-wire radiosonde temperature sensor under different solar radiation directions

parameters were held constant. The resulting surface temperature distributions and thermal equilibrium characteristics under different incident angles were analyzed. The simulation results are presented in Fig. 4.

According to the simulation results, when the sensor is illuminated by the Sun at a 45° incidence angle and the illumination direction is varied in 30° increments, the maximum change in the average temperature of the resistive element is only 0.033 K. First, the metallic coating on the sensor surface effectively reflects most of the incoming solar radiation, substantially reducing the temperature rise caused by radiative absorption. Second, the four-wire temperature sensor features a highly symmetric structure in which four metal leads support the central thermistor at uniformly spaced azimuthal angles, forming balanced heat-conduction and heat-dissipation paths in three-dimensional space. This geometric symmetry enables the sensing element to maintain an almost identical radiative thermal equilibrium under different solar incidence angles, thereby minimizing the temperature deviations induced by directional illumination. In addition, the high thermal conductivity of the metal leads rapidly spreads any localized heating along the wires, further suppressing the small temperature differences associated with varying illumination directions. This result confirms that the four-wire radiosonde temperature sensor achieves excellent radiative thermal balance in three-dimensional space, thereby significantly improving the accuracy of radiation error correction in atmospheric temperature measurements.

2.3. Impact of Different Environmental Factors on Radiation Errors

To further investigate the variation of radiation temperature errors in the four-wire radiosonde temperature sensor under different environmental conditions, a series of multiphysics coupled simulations were conducted using CFD methods. The analysis considered various combinations of altitude, ascent velocity, and solar radiation intensity. The initial temperature of both the air domain and the sensor surface was set to 300 K. Solar radiation intensities of 400 W/m^2, 600 W/m^2, 800 W/m^2, and 1000 W/m^2 were applied. The altitude was varied from 6 km to 25 km in 1 km increments, while the ascent velocity was varied from 1 m/s to 5 m/s in 1 m/s steps. The simulation results are presented in Fig. 5.

When the altitude is held constant, the radiation error increases as the ascent speed decreases. This is because the convective heat transfer around the sensor becomes weaker at lower ascent speeds, making it more difficult for the sensor to dissipate the solar energy it absorbs, thereby amplifying the resulting temperature rise. Conversely, at a fixed ascent speed, the radiation error exhibits an exponential increase with altitude. As the atmospheric density and heat capacity decrease at higher altitudes, the aerodynamic heating effect becomes significantly weaker, and the sensor's surface energy balance becomes more sensitive to solar radiation, leading to an intensified radiation-induced temperature error. In addition, stronger solar radiation further enlarges the radiation error, as the amount of absorbed radiative energy increases while the heat dissipation conditions do not improve correspondingly. Under extreme conditions — namely a solar radiation intensity of 1000 W/m^2, an ascent speed of 1 m/s, and an altitude of 25 km — the air becomes sufficiently rarefied that convective heat transfer is minimized, while the absorbed radiation reaches its maximum. As a result, the four-wire radiosonde temperature sensor experiences its highest radiation-induced temperature increase, with the radiation error reaching 0.652 K. These findings indicate that under the combined effects of strong solar radiation and high-altitude low-density air, radiation errors can significantly affect sensor measurements.

3. DESIGN OF A RADIATION ERROR CORRECTION ALGORITHM

In the preceding sections, a multi-physics coupling model was employed to investigate the influence of environmental parameters on radiation-induced measurement errors. However, in practical meteorological observations, these parameters vary dynamically and continuously over time. As a result, numerical simulations based on discrete parameter values are insufficient to capture the continuity and complexity of measurement errors under real-world conditions. To address this limitation, this study proposes a correction method based on an multilayer

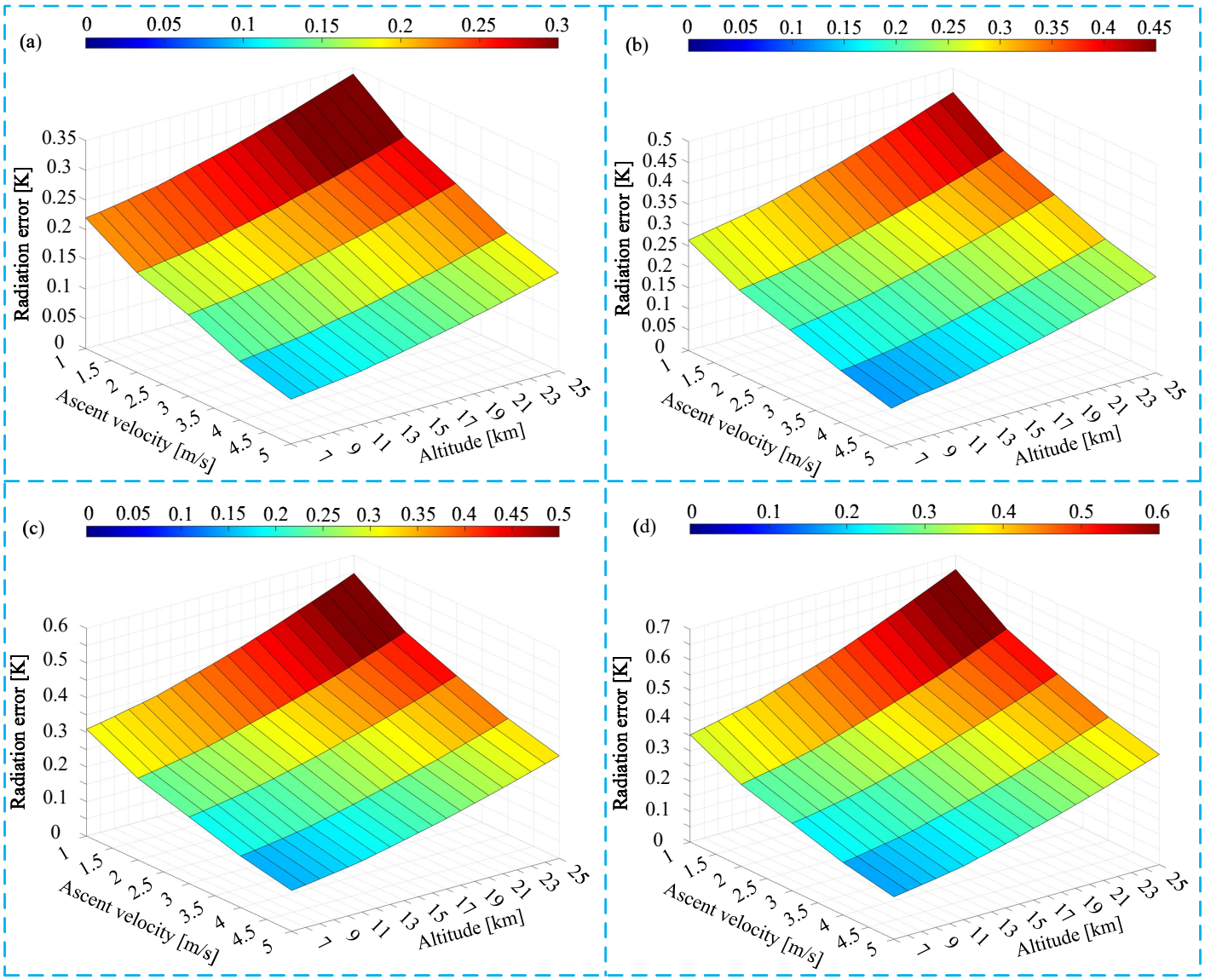

FIGURE 5. Numerical calculation results of radiation errors for the radiosonde temperature sensor under different environmental conditions. (a) Solar radiation intensity of 400 W/m^2. (b) Solar radiation intensity of 600 W/m^2. (c) Solar radiation intensity of 800 W/m^2. (d) Solar radiation intensity of 1000 W/m^2.

perceptron (MLP) neural network [29]. By taking various environmental parameters as inputs and radiation error as the output, the neural network is trained to learn a generalized correction function capable of accurately estimating measurement errors across a range of conditions.

To determine the optimal network architecture and hyperparameters — including the number of hidden layers, the number of neurons in each layer, and the activation function — a Bayesian optimization strategy was employed. The search space was defined to include 1–3 hidden layers with 1–300 neurons per layer. Each candidate configuration was evaluated through five-fold cross-validation, and the mean validation performance was used to guide the optimization process. The Bayesian optimization identified an optimal architecture consisting of two hidden layers with 12 and 17 neurons, respectively. After selecting the optimal hyperparameters, the final model was retrained on 80% of the dataset designated for training in order to obtain a unified set of model weights. The network was trained using the Adam optimizer with a learning rate of 0.0005, a batch size of 32, and 500 epochs. Convergence was assessed based on the stability of the validation loss. All input features were normalized using Z-score standardization prior to training, and 20% of the dataset was reserved for independent validation. On the validation set, the optimized model achieved an RMSE of 0.0041, an MAE of 0.0029, and an R^2 of 0.99, demonstrating excellent predictive accuracy and strong generalization capability. Therefore, this architecture was adopted as the final model for this study.As shown in Fig. 6, the optimized two-hidden-layer MLP architecture establishes a hierarchical feature-extraction mechanism for modeling the nonlinear relationship between inputs and radiation-error outputs. The computational expressions for the outputs of the two hidden layers

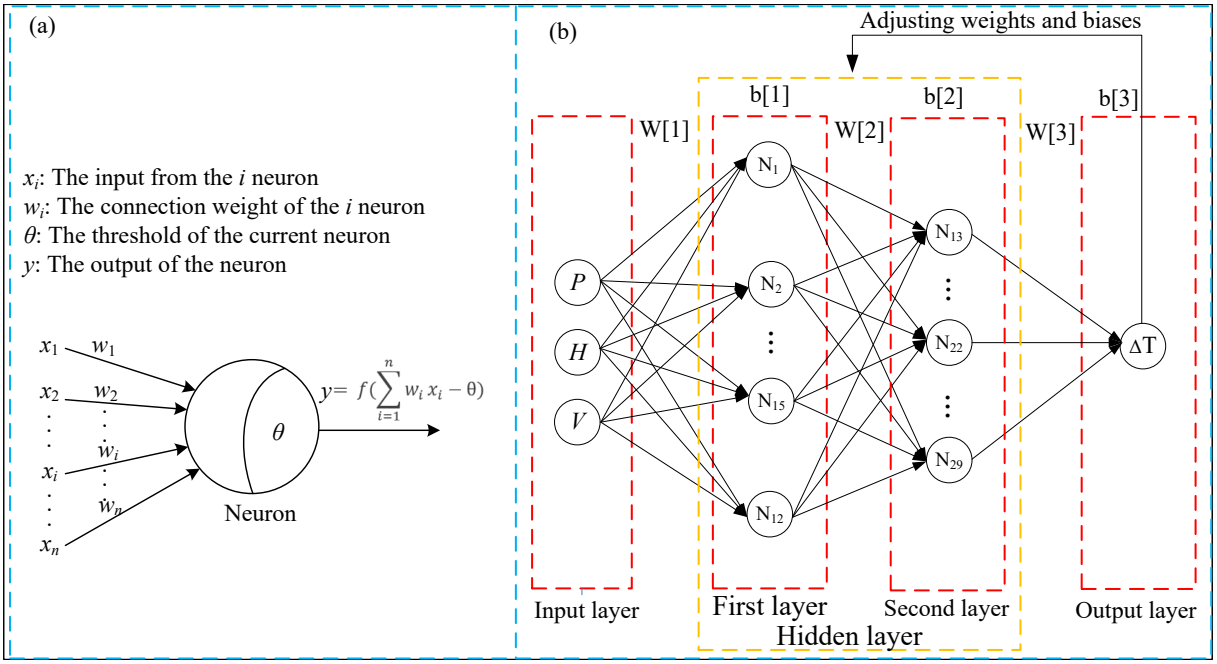

FIGURE 6. (a) Neuron model. (b) Neural network architecture diagram.

and output layer are as follows:

$$A[1] = \text{ReLU}\left(W[1]X + b[1]\right) \quad (1)$$

$$A[2] = \text{ReLU}\left(W[2]X + b[2]\right) \quad (2)$$

$$\Delta T = \text{Purelin}\left(W[3]A[2] + b[3]\right) \quad (3)$$

where $A[1]$ represents the output of the first hidden layer, which is the result of the weighted sum with weight matrix $W[1]$ and bias term $b[1]$, passed through an activation function. This output also serves as the input for the second hidden layer. $A[2]$ is the output from the second hidden layer and is used as the input to the output layer. ΔT is the output of the neural network.

The activation function employed in the hidden layers is rectified linear unit (ReLU), while the output layer utilizes the Purelin (linear) activation function. Compared with sigmoid and tanh functions, ReLU offers a significant advantage in accelerating network convergence. This is primarily because sigmoid and tanh are prone to the vanishing gradient problem, where gradients tend to zero during backpropagation, potentially hindering effective learning. In contrast, ReLU maintains a constant derivative of 1 on the positive half-axis, thereby mitigating the vanishing gradient issue [30]. The Purelin function is well-suited for regression tasks, as it does not constrain the output to a fixed range. This preserves the continuity and scalability of the predicted values, allowing the network to better approximate the actual distribution of the target variable. The ReLU activation function is defined in Eq. (4), and the Purelin activation function is defined in Eq. (5).

$$\text{ReLU}\left(x\right) = \max\left(0, x\right) \quad (4)$$

$$\text{Purelin}\left(x\right) = x \quad (5)$$

Once the MLP network structure is built, and the activation functions for each layer are selected, the neural network's computation process primarily involves two stages: forward signal propagation and backward error propagation. The forward propagation process is as follows.

The input to the i-th neuron in the hidden layer is the weighted sum of all the inputs to that neuron, plus a bias term. This can be expressed mathematically as Eq. (6).

$$net_i = \sum W_{ij} x_j + \theta_i \quad (6)$$

The output yi of the i-th neuron in the hidden layer can be expressed as Eq. (7).

$$y_i = \Phi\left(nei_i\right) \quad (7)$$

The input to the k-th neuron in the output layer, denoted as net_k, can be expressed as Eq. (8).

$$net_k = \sum_{i=1}^{q} W_{ki} y_i + \alpha_k = \sum_{i=1}^{q} W_{ki} \Phi\left(\sum_{j=1}^{M} W_{ij} x_i + \theta_i\right) + \alpha_k \quad (8)$$

The output of the k-th neuron in the output layer, denoted as O_k, can be expressed as Eq. (9).

$$O_k = \varphi(net_k) = \varphi\left[\sum_{i=1}^{q} W_{ki} \Phi\left(\sum_{j=1}^{M} W_{ji} x_j + \theta_i\right) + \alpha_k\right] \quad (9)$$

The weight connecting the i-th neuron in the hidden layer and the j-th neuron in the input layer is denoted as W_{ij}, while θ_i represents the threshold of the i-th hidden layer neuron. Similarly, the weight from the output layer neuron to the j-th hidden layer neuron is denoted as W_{ki}, and α_k represents the threshold

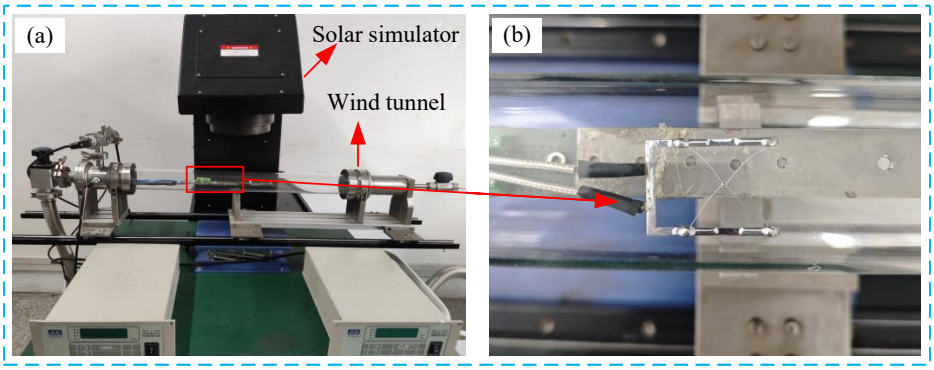

FIGURE 7. (a) Experimental platform based on the low-pressure wind tunnel and full-spectrum solar simulator. (b) Four-wire sounding temperature sensor.

of the output layer neuron. The final output of the output layer is denoted as O_k.

The error backpropagation process begins at the output layer and sequentially calculates the output error for each preceding neuron layer. This error is propagated backward through the network using the chain rule, enabling the computation of gradient information for all layers. Subsequently, an optimization strategy based on gradient descent is applied, where the weights and biases of each layer are updated using the computed gradients and a predefined learning rate. Through iterative cycles of error backpropagation and parameter adjustment, the neural network progressively learns the mapping relationship between the input features and the output target. After sufficient training, the network is capable of generating predictions that closely approximate the true values, thereby demonstrating strong generalization capability.

The quadratic error criterion function for a single sample P is defined as Eq. (10).

$$E_p = \frac{1}{2}\sum_{k=1}^{L}(T_k - O_k)^2 \tag{10}$$

The total error criterion function for all P samples in the neural network is defined as Eq. (11).

$$E = \frac{1}{2}\sum_{p=1}^{p}\sum_{k=1}^{L}(T_k^p - O_k^p)^2 \tag{11}$$

To minimize the error function, the gradient descent method is used to optimize the network parameters. Specifically, the backpropagation algorithm is used to compute the adjustments for the weights and biases of the output layer and hidden layers. The update formulas for the output layer weights ΔW_{ki}, output layer biases $\Delta\alpha_k$, hidden layer weights ΔW_{ij}, and hidden layer biases $\Delta\theta_i$ are as Eqs. (12)–(15).

$$\Delta\omega_{ki} = \eta\sum_{p=1}^{p}\sum_{k=1}^{L}(T_k^p - O_k^p)\cdot\Psi'(net_k)\cdot y_i \tag{12}$$

$$\Delta\alpha_{ki} = \eta\sum_{p=1}^{p}\sum_{k=1}^{L}(T_k^p - O_k^p)\cdot\Psi'(net_k) \tag{13}$$

$$\Delta\omega_{ij} = \eta\sum_{p=1}^{p}\sum_{k=1}^{L}(T_k^p - O_k^p)\cdot\Psi'(net_k)\cdot\omega_{ki}\varphi'(net_i)\cdot x_i \tag{14}$$

$$\Delta\theta_i = \eta\sum_{p=1}^{p}\sum_{k=1}^{L}(T_k^p - O_k^p)\cdot\Psi'(net_k)\cdot\omega_{ki}\cdot\varphi'\cdot(net_i) \tag{15}$$

Based on Eqs. (12)–(15), the weights and biases of the network can be iteratively adjusted using the Eqs. (16)–(19).

$$\omega_{ki}(k+1) = \omega_{ki}(k) + \Delta\omega_{ki}(k) \tag{16}$$

$$\omega_{ij}(k+1) = \omega_{ij}(k) + \Delta\omega_{ij}(k) \tag{17}$$

$$\alpha_k(k+1) = \alpha_k(k) + \Delta\alpha_k(k) \tag{18}$$

$$\theta_i(k+1) = \theta_i(k) + \Delta\theta_i(k) \tag{19}$$

In this model, the outputs of the hidden layer neurons are treated as independent variables, while the outputs of the output layer neurons serve as dependent variables. The training process is iterative, continuing until the network output error converges to a predefined threshold or meets other stopping criteria. Based on the simulation results shown in Fig. 5, training samples are established, and the MLP neural network algorithm is employed for learning.

4. EXPERIMENTAL STUDY

4.1. Experimental Platform Setup

A laboratory observation platform was constructed by integrating a low-pressure wind tunnel with a full-spectrum AM1.5G solar radiation simulator. Solar radiation was provided by the AM1.5G simulator, which covers a wavelength range of 300–1100 nm and employs a xenon arc lamp as the light source. Under standard operating conditions, the simulator closely reproduces the spectral distribution and intensity of natural sunlight, ensuring uniform and stable irradiation of the four-wire radiosonde temperature sensor. The irradiation intensity was adjustable from 100 W/m^2 to 1200 W/m^2, enabling precise replication of the solar heating effects experienced during high-altitude ascents. The low-pressure wind tunnel was capable of operating at pressures ranging from 50 Pa to 100 kPa. Internal pressure was regulated through an adjustable valve and

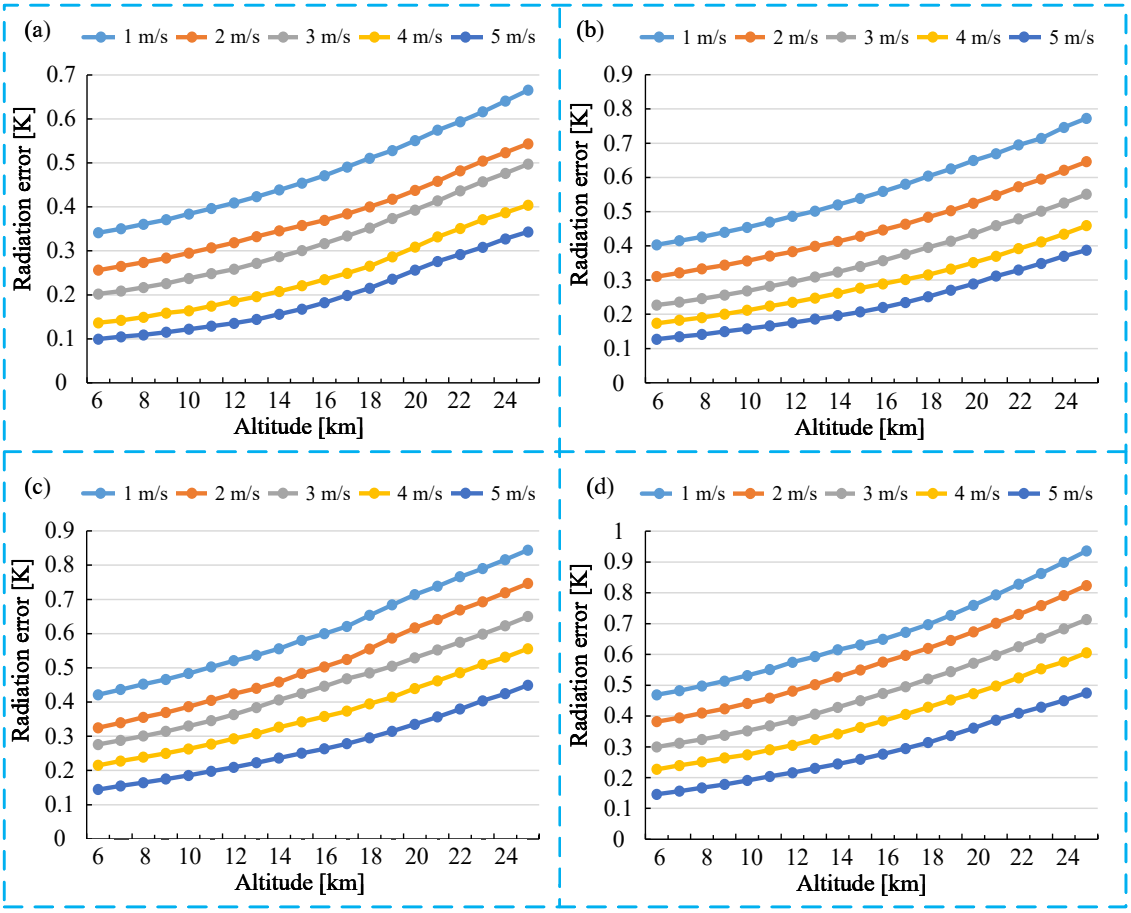

FIGURE 8. Relationship among radiation intensity, altitude, ascent speed, and radiation error under different conditions. (a) Solar radiation intensity of 400 W/m^2. (b) Solar radiation intensity of 600 W/m^2. (c) Solar radiation intensity of 800 W/m^2. (d) Solar radiation intensity of 1000 W/m^2.

continuously monitored with a vacuum gauge. The airflow velocity could be varied between 1 and 7 m/s and was measured using a high-precision flowmeter. This configuration allowed accurate simulation of atmospheric conditions and sensor ascent through the upper troposphere and lower stratosphere under controlled wind speeds.During the experiments, the four-wire radiosonde temperature sensor was mounted at the center of the low-pressure wind tunnel and positioned directly beneath the solar simulator. The lead-wire plane was oriented perpendicular to the incident radiation to ensure uniform exposure. The complete experimental setup is illustrated in Fig. 7.

4.2. Experimental Parameter Settings

The altitude range is set from 6 to 25 km, with a step size of 1 km. The solar radiation intensity is set to 400 W/m^2, 600 W/m^2, 800 W/m^2, and 1000 W/m^2. The low-pressure wind tunnel provides an air speed range from 1 to 5 m/s, with a step size of 1 m/s. A total of 400 experimental runs were conducted, with the environmental parameters set as shown in Table 3.

4.3. Experimental Data Analysis

The experimental data of radiation errors for the four-lead radiosonde temperature sensor under different environmental

TABLE 3. Environmental parameter settings.

Sample No.	Radiation intensity (W/m^2)	Altitude (km)	Wind speed (m/s)
1–100	400	6–25	1–5
101–200	600	6–25	1–5
201–300	800	6–25	1–5
301–400	1000	6–25	1–5

conditions are shown in Fig. 8. The experimental results exhibit the same overall trend as the CFD simulations, although the measured radiation errors are slightly higher. This discrepancy may result from idealized assumptions in the CFD model, such as perfectly uniform geometry and coating, as well as real-world effects including flow turbulence in the wind tunnel, fluctuations in the solar simulator output, and minor variations in ambient pressure.

Under constant solar radiation intensity, the radiation error of the four-wire radiosonde temperature sensor increases with altitude. Conversely, when the altitude is fixed, a higher ascent speed leads to a reduction in radiation error. Specifically, under conditions of 1000 W/m^2 solar radiation intensity, an altitude of 25 km, and an ascent speed of 1 m/s, the maximum ra-

diation error reaches 0.936 K. At the same radiation intensity, the maximum variation in radiation error across different ascent speeds is 0.461 K. This result indicates that airflow velocity has a significant impact on radiation error, as increased airflow enhances convective heat transfer on the sensor surface, thereby reducing the error.

The main sources of uncertainty include the thermistor's intrinsic accuracy, wind tunnel airflow velocity and turbulence, ambient pressure fluctuations, stability and spectral variations of the solar simulator, repeatability errors of the measurement system, sensor mounting deviations, and data acquisition noise. All measurement instruments were calibrated prior to the experiments, and the measurement uncertainties were assumed to remain statistically stable throughout the entire process, without introducing systematic drift. Combined using the root-sum-square method, these uncertainties yield an expanded uncertainty of 0.18 K ($k = 2$, 95% confidence level).

The environmental parameters listed in Table 2 are used as input neurons for the previously established correction algorithm. The algorithm is employed to fit the radiation error under varying environmental conditions. The corrected error is obtained by calculating the difference between the fitted radiation error and the experimentally measured value. Fig.9 presents the experimental radiation error, the values corrected using the neural network model, and the corresponding residual errors for the four-wire temperature sensor. Under the same airflow velocity, the residual error after correction increases with altitude because the decreasing air density at higher altitudes weakens convective heat transfer, reducing the sensor's ability to dissipate absorbed solar radiation. In contrast, at a fixed altitude, the residual error decreases as the ascent speed increases, as higher airflow enhances forced convection around the sensor surface and suppresses radiation-induced heating. Moreover, micro-radiation intensity remains the most direct factor influencing the corrected error: stronger radiation leads to greater radiative heating of the sensor, thereby enlarging the temperature deviation that the correction algorithm must compensate for and consequently resulting in larger residuals under high-radiation conditions.

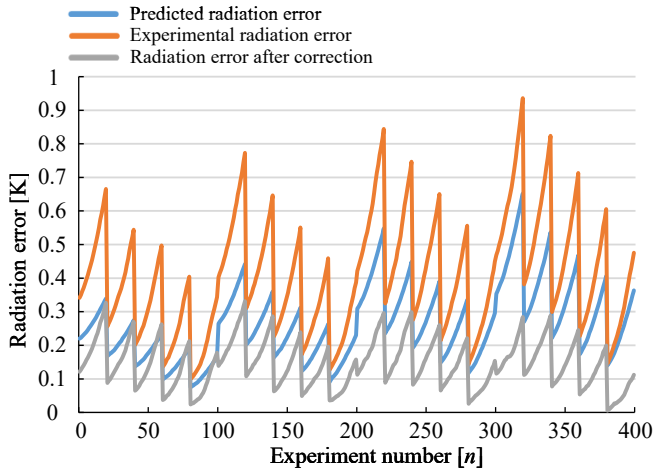

FIGURE 9. Comparison of experimental radiation error, predicted radiation error, and radiation error after correction of the four-wire sounding temperature sensor.

To evaluate the accuracy of the predicted radiation error results, the root mean square error (RMSE), mean absolute error (MAE), and correlation coefficient (r) are introduced, with the corresponding formulas provided in Eqs. (20)–(22).

$$RMSE = \sqrt{\frac{\sum_{i=1}^{n}(x_i - y_i)^2}{n}} \tag{20}$$

$$MAE = \frac{1}{n}\sum_{i=1}^{n} | x_i - y_i | \tag{21}$$

$$r = \frac{\sum_{i=1}^{n}(x_i - \overline{x}) \cdot (y_i - \overline{y})}{\sqrt{\sum_{i=1}^{n}(x_i - \overline{x})^2} \cdot \sqrt{\sum_{i=1}^{n}(y_i - \overline{y})^2}} \tag{22}$$

where x_i and y_i represent the experimental radiation errors and predicted radiation errors of the temperature measurement system, respectively, while $\overline{x}$ and $\overline{y}$ denote the corresponding means, and n is the sample size.

As shown in Fig. 9, the neural network was employed to correct the radiation error of the four-wire sounding temperature sensor using 400 sets of experimental data. Before correction, the average radiation error of the sensor was 0.446 K. After applying the correction algorithm, the RMSE, MAE, and correlation coefficient between the experimental radiation error and the neural network-fitted values were 0.159 K, 0.143 K, and 0.962, respectively. The 95% confidence interval for the radiation error after correction ranged from 0.136 K to 0.150 K. These results indicate that the neural network-based correction algorithm provides high correction accuracy, with an average post-correction error reduced to the order of 0.1 K.However, reducing the error to this level in the laboratory does not guarantee equivalent performance in real-world sounding flights, where factors such as solar elevation angle, ventilation rate, ascent velocity, atmospheric turbidity, cloud cover, and sensor aging may alter the radiation environment. Therefore, the 0.1 K accuracy reported here should be interpreted as the achievable performance under laboratory conditions, and its applicability to operational soundings requires further validation through field experiments across diverse atmospheric conditions.

5. CONCLUSION

This study proposes a four-wire structural design for the radiosonde temperature sensor and evaluates its performance through CFD simulations. A coupled flow-structure thermal analysis is conducted under varying environmental conditions, including altitude, ascent velocity, and solar radiation intensity, to quantify the radiation error of the four-wire sensor. A neural network algorithm is then trained on the simulation data to develop a radiation error correction model. Experimental validation is performed using a platform comprising a full-spectrum solar simulator and a low-pressure wind tunnel.The main contributions, limitations, and future research directions are summarized as follows:

(1) The four-wire lead structure exhibits excellent radiation heat balance in three-dimensional space, with minimal variation in radiation levels. As a result, the influence of solar radiation direction on measurement accuracy is negligible, allowing

the error correction process to be simplified by omitting directional considerations.

(2) The measurement error of the four-wire sounding temperature sensor increases with both altitude and solar radiation intensity. However, the direction of solar radiation has little effect on the error. Wind speed significantly influences the radiation error, with higher wind speeds enhancing convective heat transfer and thereby reducing the measurement error.

(3) Before applying the correction algorithm, the average radiation-induced observation error of the sensor was 0.446 K. After correction using the proposed neural network-based approach, the average error was effectively reduced to the order of 0.1 K.

(4) Although the laboratory environment incorporates low-pressure, high-irradiance, and controlled-flow conditions, it still cannot fully reproduce the complexity of real-world flights. Furthermore, because the correction model is trained primarily on CFD-generated data, its performance may degrade when actual atmospheric conditions deviate from the simulated parameter space.

(5) Future work will expand the simulation scenarios to cover a wider range of solar elevation angles, dynamic radiative fluxes, and more realistic atmospheric compositions, while incorporating additional real radiosonde flight datasets to enhance model generalization under true high-altitude conditions. In addition, real radiosonde flight experiments will be conducted to further validate the correction model and assess its performance under actual atmospheric conditions.

REFERENCES

[1] Watt-Meyer, O., N. D. Brenowitz, S. K. Clark, B. Henn, A. Kwa, J. McGibbon, W. A. Perkins, and C. S. Bretherton, "Correcting weather and climate models by machine learning nudged historical simulations," *Geophysical Research Letters*, Vol. 48, No. 15, e2021GL092555, 2021.

[2] Xu, Y., V. Ramanathan, and D. G. Victor, "Global warming will happen faster than we think," *Nature*, Vol. 564, No. 7734, 30–32, 2018.

[3] Balanyá, J., J. M. Oller, R. B. Huey, G. W. Gilchrist, and L. Serra, "Global genetic change tracks global climate warming in drosophila subobscura," *Science*, Vol. 313, No. 5794, 1773–1775, 2006.

[4] Scher, S. and G. Messori, "How global warming changes the difficulty of synoptic weather forecasting," *Geophysical Research Letters*, Vol. 46, No. 5, 2931–2939, 2019.

[5] Joseph, J. J., R. Meenal, F. T. Josh, P. A. Michael, V. K. Krishnamoorthy, G. Chandran, and S. Veerabathran, "Weather observation and forecasting using radiosonde," *Telkomnika (Telecommunication Computing Electronics and Control)*, Vol. 20, No. 6, 1376–1383, 2022.

[6] Free, M., I. Durre, E. Aguilar, D. Seidel, T. C. Peterson, R. E. Eskridge, J. K. Luers, D. Parker, M. Gordon, J. Lanzante, et al., "Creating climate reference datasets: CARDS workshop on adjusting radiosonde temperature data for climate monitoring," *Bulletin of the American Meteorological Society*, Vol. 83, No. 6, 891–900, 2002.

[7] Free, M., D. J. Seidel, J. K. Angell, J. Lanzante, I. Durre, and T. C. Peterson, "Radiosonde Atmospheric Temperature Products for Assessing Climate (RATPAC): A new data set of large-area anomaly time series," *Journal of Geophysical Research: Atmospheres*, Vol. 110, No. D22, 2005.

[8] World Meteorological Organization, *Guide to Meteorological Instruments and Methods of Observation*, Secretariat of the World Meteorological Organization, 1983.

[9] Li, Z., L. Chang, J. Lou, Y. Shen, and H. Yan, "Multi-scale analysis of the relationships between solar activity, CO_2 and global surface temperature," *Research in Astronomy and Astrophysics*, Vol. 22, No. 9, 095019, 2022.

[10] Heyd, R., "One-dimensional systemic modeling of thermal sensors based on miniature bead-type thermistors," *Sensors*, Vol. 21, No. 23, 7866, 2021.

[11] Segales, A. R., P. B. Chilson, and J. L. Salazar-Cerreño, "Considerations for improving data quality of thermo-hygrometer sensors on board unmanned aerial systems for planetary boundary layer research," *Atmospheric Measurement Techniques*, Vol. 15, No. 8, 2607–2621, 2022.

[12] Liu, Y., J. Wang, P. Huo, C. Shi, Z. Liu, Y. Yan, J. Yao, and A. Chang, "A novel design of fast response Mn-Ni-Cu-Fe-O microbead thermistors for radiosonde," *Journal of Materials Science: Materials in Electronics*, Vol. 34, No. 24, 1737, 2023.

[13] Wang, G., C. Hu, and D. Zheng, "Theoretical and simulation analysis of a thin film temperature sensor error model for in situ detection in near space," *Applied Sciences*, Vol. 13, No. 10, 5954, 2023.

[14] Kottmeier, C., A. Wieser, U. Corsmeier, N. Kalthoff, P. Gasch, B. Kirsch, D. Ebert, Z. Ulanowski, D. Schell, H. Franke, F. Schmidmer, J. Frielingsdorf, T. Feuerle, and R. Hankers, "A new versatile dropsonde for atmospheric soundings–the KITsonde," *Atmospheric Measurement Techniques*, Vol. 18, No. 13, 3161–3178, 2025.

[15] Abdunabiev, S., C. Musacchio, A. Merlone, M. Paredes, E. Pasero, and D. Tordella, "Validation and traceability of miniaturized multi-parameter cluster radiosondes used for atmospheric observations," *Measurement*, Vol. 224, 113879, 2024.

[16] Lee, S.-W., E. U. Park, B. I. Choi, J. C. Kim, S.-B. Woo, S. Park, S. G. Yang, and Y.-G. Kim, "Dual temperature sensors with different emissivities in radiosondes for the compensation of solar irradiation effects with varying air pressure," *Meteorological Applications*, Vol. 25, No. 1, 49–55, 2018.

[17] Lee, S.-W., S. Kim, Y.-S. Lee, J.-K. Yoo, S. Lee, S. Kwon, B. I. Choi, J. So, and Y.-G. Kim, "Laboratory characterisations and intercomparison sounding test of dual thermistor radiosondes for radiation correction," *Atmospheric Measurement Techniques*, Vol. 15, No. 8, 2531–2545, 2022.

[18] Lee, S.-W., S. Kim, Y.-S. Lee, B. I. Choi, W. Kang, Y. K. Oh, S. Park, J.-K. Yoo, J. Lee, S. Lee, S. Kwon, and Y.-G. Kim, "Radiation correction and uncertainty evaluation of RS41 temperature sensors by using an upper-air simulator," *Atmospheric Measurement Techniques*, Vol. 15, No. 5, 1107–1121, 2022.

[19] Sun, X., S. Yan, B. Wang, L. Xia, Q. Liu, and H. Zhang, "Air temperature error correction based on solar radiation in an economical meteorological wireless sensor network," *Sensors*, Vol. 15, No. 8, 18 114–18 139, 2015.

[20] Wang, B., X. Gu, L. Ma, and S. Yan, "Temperature error correction based on BP neural network in meteorological wireless sensor network," *International Journal of Sensor Networks*, Vol. 23, No. 4, 265–278, 2017.

[21] Von Rohden, C., M. Sommer, T. Naebert, V. Motuz, and R. J. Dirksen, "Laboratory characterisation of the radiation temperature error of radiosondes and its application to the GRUAN data processing for the Vaisala RS41," *Atmospheric Measurement Techniques*, Vol. 15, No. 2, 383–405, 2022.

[22] Jing, X., X. Shao, T.-C. Liu, and B. Zhang, "Comparison of gruan rs92 and rs41 radiosonde temperature biases," *Atmosphere*, Vol. 12, No. 7, 857, 2021.

[23] Yang, J., J. Jiang, R. Ding, and Q. Liu, "Design of a high-accuracy air temperature measurement system using computational fluid dynamics and neural networks," *International Journal of Thermal Sciences*, Vol. 214, 109895, 2025.

[24] Luza, L. M., A. Ruospo, D. Söderström, C. Cazzaniga, M. Kastriotou, E. Sanchez, A. Bosio, and L. Dilillo, "Emulating the effects of radiation-induced soft-errors for the reliability assessment of neural networks," *IEEE Transactions on Emerging Topics in Computing*, Vol. 10, No. 4, 1867–1882, 2022.

[25] Vivarelli, G., N. Qin, and S. Shahpar, "A review of mesh adaptation technology applied to computational fluid dynamics," *Fluids*, Vol. 10, No. 5, 129, 2025.

[26] Aguerre, H. J., P. H. Pedreira, P. J. Orbaiz, and N. M. Nigro, "Validation and enhancement of a supermesh strategy for the CFD simulation of four-stroke internal combustion engines," *Fluids*, Vol. 7, No. 3, 104, 2022.

[27] Aycan, O., A. Topuz, and L. Kadem, "Evaluating uncertainties in CFD simulations of patient-specific aorta models using Grid Convergence Index method," *Mechanics Research Communications*, Vol. 133, 104188, 2023.

[28] Abdelrazik, A. S., A. Osama, A. N. Allam, B. Shboul, M. A. Sharafeldin, M. Elwardany, and A. M. Masoud, "ANSYS-Fluent numerical modeling of the solar thermal and hybrid photovoltaic-based solar harvesting systems," *Journal of Thermal Analysis and Calorimetry*, Vol. 148, No. 21, 11 373–11 424, 2023.

[29] Jin, W., X. Hong, J. Yang, Q. Liu, Z. Li, Q. Ding, and H. M. Amdadul, "Development of a high-accuracy temperature sensor for meteorological observations based on computational fluid dynamics and neural networks," *International Communications in Heat and Mass Transfer*, Vol. 164, 108801, 2025.

[30] Hu, Z., J. Zhang, and Y. Ge, "Handling vanishing gradient problem using artificial derivative," *IEEE Access*, Vol. 9, 22 371–22 377, 2021.